INORGANIC CHEMISTRY FRONTIERS

RESEARCH ARTICLE

View Article Online
View Journal | View Issue

Cite this: *Inorg. Chem. Front.*, 2023, **10**, 2115

A UiO-66-NH_2 MOF derived N doped porous carbon and ZrO_2 composite cathode for zinc-ion hybrid supercapacitors†

Xiaoqi Wang, [a,c] Hu Hong,[b] Shuo Yang,[b] Shengchi Bai,[c] Rui Yang,[c] Xu Jin,[c] Chunyi Zhi *[b] and Bo Wang *[a]

Aqueous Zn-ion hybrid supercapacitors (ZHSs) integrating the merits of Zn-ion batteries with high energy densities and supercapacitors with high power densities are considered one of the promising candidates for highly safe large-scale energy storage. Unfortunately, the unsatisfactory energy density of carbon-based cathode materials limited the practical application of ZHSs. A strategy of introducing heteroatoms and pseudocapacitive metal oxide materials into carbon materials is proposed to build ZHSs with better electrochemical performance. Herein, an N-doped carbon framework with homogeneously distributed nanoscale ZrO_2 (NC@ZrO_2) was prepared by pyrolyzing Zr-containing metal–organic frameworks (MOFs, UiO-66-NH_2). Due to the facilitated chemical adsorption and accelerated Zn^{2+}-storage kinetics, the NC@ZrO_2-based ZHS demonstrates a remarkable maximum energy density of 69 W h kg^{-1} and a maximum power density of 5760 W kg^{-1}. This work provides a promising strategy to fabricate high-performance cathode materials for ZHSs by integrating the N-doping strategy and pseudocapacitive reactions, which sheds light on the charge-storage mechanism and advanced cathode material design for ZHSs toward practical applications.

Received 1st January 2023,
Accepted 9th February 2023

DOI: 10.1039/d2qi02777a

rsc.li/frontiers-inorganic

1. Introduction

Aqueous Zn-ion hybrid supercapacitors (ZHSs) integrating the high energy density of aqueous zinc batteries (AZIBs)[1–4] and the high power density of supercapacitors[5–8] are suitable for various electrochemical energy storage scenarios.[5–12] The fundamental chemistry of ZHSs is based on the reversible electrodeposition of Zn^{2+} on the anode side and the adsorption/de-adsorption process on the cathode side. Compared with the Zn anode showing a low redox potential (−0.76 V *vs.* standard hydrogen) and a high theoretical specific capacity (823 mA h g^{-1} or 5855 mA h cm^{-3}), the development of carbon-based cathode materials is hindered by the unsatisfactory Zn^{2+} storage capability.[13–15] Great efforts have been made to achieve higher energy density with carbon-based cathode materials, including regulating the micro-structure and pore size, doping with heteroatoms,[5,16] and introducing pseudocapacitive materials.[6] Among various optimization strategies, heteroatom doping is a facile and effective strategy to enhance the Zn^{2+} storage capability of carbon-based materials. Introducing heteroatoms in carbon may lead to lattice defects, which provide additional active sites and enhance the conductivity of carbon. Besides, the ameliorated surface tensile and adsorption properties of doped carbon boost the redox reaction on the cathode surface. Nitrogen atoms, which show a similar radius to carbon and higher electronegativity, are regarded as promising heteroatoms to improve the electrochemical performance of carbon-based materials.

Introducing pseudocapacitive materials into carbon-based materials is another way that has been demonstrated to be effective in improving the energy density of ZHSs. The reversible redox reaction on the surface of pseudocapacitive materials endows them with significantly higher capacitances while retaining fast reaction kinetics.[17] Several types of pseudocapacitive materials have been reported with good electrochemical performance, including conducting polymers,[18,19] MXenes,[9,20] and transition metal oxides (TMOs)[21] or nitrides,[6] among which TMOs have drawn tremendous attention in supercapacitors owing to the advantages of

[a]*School of Chemistry and Chemical Engineering, Beijing Institute of Technology, Beijing 100081, China. E-mail: bowang@bit.edu.cn*
[b]*Department of Materials Science and Engineering, City University of Hong Kong, 83 Tat Chee Avenue, Kowloon, Hong Kong SAR, China. E-mail: cy.zhi@cityu.edu.hk*
[c]*Research Institute of Petroleum Exploration & Development (RIPED), China National Petroleum Corporation, Beijing, 100083, China*

† Electronic supplementary information (ESI) available. See DOI: https://doi.org/10.1039/d2qi02777a

natural abundance, low cost, and rich redox reactions. The biggest problem that hinders the practical application of TMOs is their relatively lower electronic conductivity. For example, zirconium oxide (ZrO_2), which shows higher conductivity than other TMOs like TiO_2 and MnO_2, still suffers from high resistance at room temperature (3.16×10^{13}–3.16×10^{18} Ω m).[22] As a result, the electrochemical performances of pure TMOs are far from satisfactory, with both limited capacitance and poor rate capability achieved. The adoption of TMOs in ZHSs relies on a conductive carbon network to address their intrinsic low conductivities. The development of nanotechnology, which reduces the size of materials into a nanoscale, provides a facile solution to enhance the electrochemical performance of TMOs by enabling good contact with the electrolyte and ensuring fast ion diffusion. For example, the nanoscale ZrO_2 (2–3 nm) has been demonstrated to provide 2.1 times higher specific capacitance than its bulky part in alkaline solutions.[23] Therefore, incorporating nanoscale ZrO_2 with the pseudocapacitive reaction into an N-doped carbon framework with a hierarchical architecture may help in obtaining high-performance ZHSs.

Herein, we report a novel cathode material for ZHSs comprising an N-doped hierarchical porous carbon framework and the homogeneously dispersed nano-sized ZrO_2 particles (NC@ZrO_2). The NC@ZrO_2 composite is prepared by direct pyrolysis of UiO-66-NH_2 with the amino functional group under a N_2 atmosphere, and it displays a large specific surface area of 269.74 m^2 g^{-1}, suitable pore-size distribution, and sufficient active sites. Due to the promoted chemical adsorption and the accelerated Zn^{2+}-storage kinetics, the NC@ZrO_2 cathode delivers remarkable electrochemical properties for ZHSs in terms of excellent capacity (81.5 mA h g^{-1}) and rate performance (45.0 mA h g^{-1} at 6.4 A g^{-1}). Furthermore, the NC@ZrO_2-based ZHS demonstrates an ultralong lifespan and superior anti-self-discharge behavior. This work provides a promising strategy to build high-performance carbon-based cathodes with the heteroatom doping strategy and pseudocapacitive reactions, which sheds light on the charge-storage mechanism and advanced materials design for ZHSs toward practical applications.

2. Experimental

2.1 The synthesis process of UiO-66 and UiO-66-NH_2 MOF

For UiO-66, $ZrCl_4$ (4 mmol) and 1,4-benzenedicarboxylic acid (H_2BDC, 8 mmol) were dissolved in a mixed solution of *N*,*N*′-dimethylformamide (DMF) (24 ml) and concentrated HCl (0.67 ml). The obtained solution was sealed in a 50 ml Teflon-lined stainless-steel autoclave and heated at 220 °C for 16 h. After cooling the vessel, white powders were obtained. The resulting solid was then filtered and purified with DMF and EtOH at room temperature several times. Similarly, UiO-66-NH_2 was synthesized and purified through the same method except for replacing the original BDC ligand with the 2-aminoterephthalic acid (NH_2-H_2BDC) ligand.

2.2 The synthesis process of NC@ZrO_2 and C@ZrO_2 composites

The as-synthesized UiO-66-NH_2 powders and UiO-66 powders were both calcined under a nitrogen atmosphere at 700 °C for 3 h with a heating rate of 10 °C min^{-1}. Then, the obtained products were put in a three-necked flask with 50 mL aqua regia and stirred at 60 °C for 24 h. After that, NC@ZrO_2 and C@ZrO_2 powders were washed with deionized water three times and dried at 80 °C overnight.

2.3 Material characterization

Powder X-ray diffraction (PXRD) data were recorded on a Rigaku Smart lab instrument operating at 40 kV voltage and 100 mA current with monochromatized Cu-Kα radiation (λ = 1.54056 Å), with a scan step of 10° min^{-1} and a scan range between 2.6° and 70°. Raman spectroscopy was carried out with 532 nm excitation using a HORIBA Scientific LabRAM HR Evolution Raman spectrometer. X-ray photoelectron spectroscopy (XPS) was performed on a Thermo Fisher Scientific K-Alpha spectrometer with Al Kα radiation to characterize the surface components. N_2 adsorption and desorption were conducted at 77.35 K using the Micromeritics Instrument ASAP 2460 after pretreating samples by heating under vacuum at 120 °C for 6 h. Pore volume and size analyses were performed by Brunauer–Emmett–Teller (BET) and Barrett–Joyner–Halenda (BJH) methods, respectively. The morphology images of MOF particles, NC@ZrO_2 and C@ZrO_2 composites were observed on a JSM-7610F field-emission scanning electron microscope (FE-SEM). A Tecnai G2 F20 transmission electron microscope (TEM) equipped with an X-ray energy-dispersive spectrometer (EDS) system operated at 200 kV accelerating voltage was applied for high-resolution transmission electron microscopy (HRTEM) imaging and composition analysis. The content of ZrO_2 in NC@ZrO_2 and C@ZrO_2 composites was analyzed using a NETZSCH STA 449F5 Thermo Gravimetric Analysis (TGA) instrument using TG-DTA mode, the samples were dried and then tested under an oxidizing atmosphere, using O_2 (20 ml min^{-1}) and N_2 (30 ml min^{-1}) as sweep gas and N_2 (20 ml min^{-1}) as protective gas, and the temperature was first raised up to 800 °C with a heating rate of 10 °C min^{-1}, and then kept at 800 °C for 10 minutes.

2.4 Electrochemical measurement

For the electrochemical measurements, cathodes were fabricated by coating the active material, Ketjenblack, and poly (vinylidene fluoride) (PVDF) with a mass ratio of 70 : 20 : 10 onto the carbon cloth. Then, the carbon cloth was dried at 80 °C overnight and cut into round disks with a diameter of 12 mm. The electrochemical behaviors of MOF-derived carbon were tested using a coin cell, in which Zn foil was used as the reference and counter electrode, and a solution of 2 M $ZnSO_4$ was used as the electrolyte. The cyclic voltammetry test was all carried out using the CHI 760D electrochemical workstation. The pseudocapacitive contribution analysis of the composite was studied using the following procedure.[24] The relationship

of the peak current (i) and the scan rate (v) obeys a power law:

$$i = av^b$$

where the b value can be calculated using the slope of the log (i) *versus* log(v) plot, where the b value of 0.5 indicates diffusion-controlled behavior and 1.0 represents the pseudocapacitive effect. The contributions to the capacity can be further quantified using the following equation:

$$i = k_1 v + k_2 v^{1/2}$$

where $k_1 v$ and $k_2 v^{1/2}$ represent the pseudocapacitive and diffusion-controlled contribution, respectively. Galvanostatic charge–discharge and self-discharge performance were analysed on the Land cell test system.

3. Results and discussion

3.1 Characterization of samples

Fig. 1 shows the preparation process of the NC@ZrO_2 composite. First, the UiO-66-NH_2 precursor was synthesized by a solvothermal method using $ZrCl_4$ and the 2-aminoterephthalic acid ligand. After that, the resulting material was pyrolyzed under a N_2 atmosphere to form a nitrogen-doped hierarchical porous carbon framework with homogeneously distributed ZrO_2 particles, followed by an acid etching process to reduce the particle size of ZrO_2 to ensure the hierarchical porous structure. For comparison, UiO-66 was synthesized by a similar method and a porous carbon framework with homogeneously distributed ZrO_2 particles was also fabricated and used as a control.

X-ray diffraction (XRD) measurement was carried out to investigate the crystal structure of the as-synthesized materials. As shown in Fig. S1,† the diffraction peaks of UiO-66-NH_2 and UiO-66 correspond well to previous reports,[25,26] confirming the formation of the desired crystalline frameworks. After calcination (Fig. 2a), the diffraction peaks corresponding to the pristine MOFs disappear, while the new peaks at 30.4°, 35.3°, 50.7°, and 60.4° demonstrate the formation of nano-sized ZrO_2 in the NC@ZrO_2 and C@ZrO_2 composites (PDF:#03-0640). The broad weak peak at 24.7° could be indexed to the (002) planes of graphitic carbon.[27] Moreover, the diffraction peaks have a broad full width at half maximum (FWHM), implying that the crystallite size is in the nanometer range. The average crystallite sizes for ZrO_2 in the NC@ZrO_2 and C@ZrO_2 composite are calculated using the Scherrer formula to be ~3.02 nm and ~3.57 nm, respectively, and the tiny difference may result from the acid etching process.

The Raman spectra in Fig. 2b show the characteristic D band (1354 cm^{-1}) and G band (1588 cm^{-1}) for both the NC@ZrO_2 and C@ZrO_2 composites, which is related to the lattice defect for defective/distorted carbon and the in-plane stretching vibration of sp^2 hybridization for graphitic carbon, respectively.[5,14,16,27,28] The degree of graphitic disorder and the defect concentration can be quantitatively evaluated by the peak area ratio of the D band to the G band (*i.e.*, I_D/I_G).[14] The I_D/I_G value of the NC@ZrO_2 composite (I_D/I_G = 1.04) is much larger than that of the C@ZrO_2 composite (I_D/I_G = 0.89), which

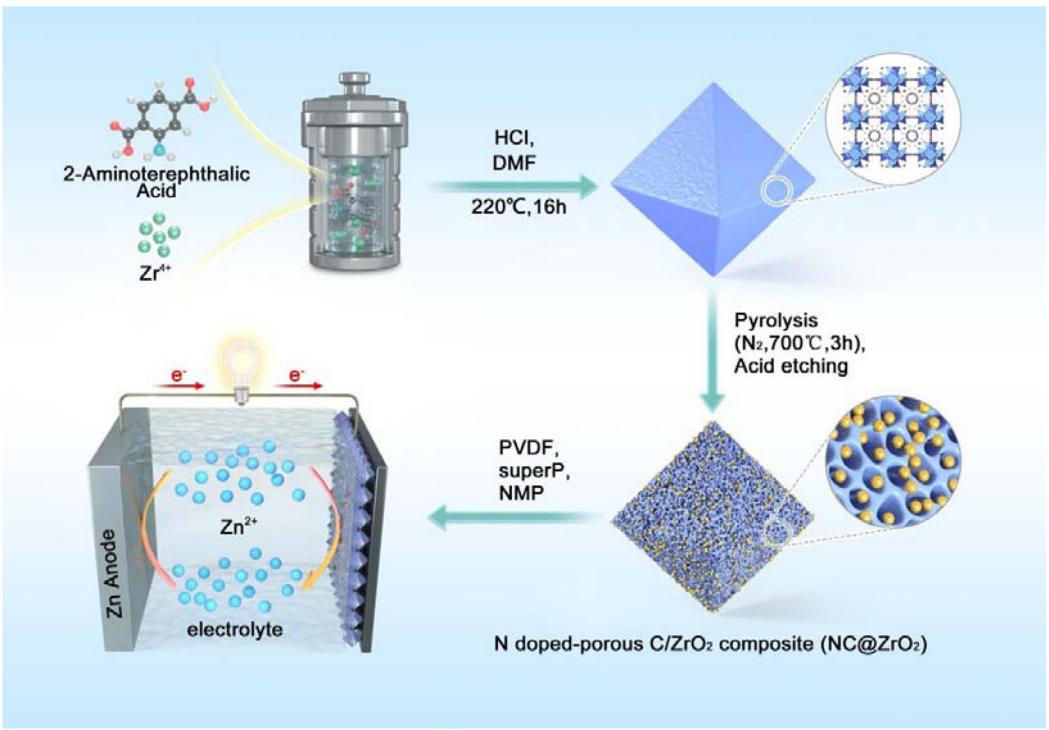

Fig. 1 Schematic illustration of the synthetic process for the NC@ZrO_2 composite and the fabricated ZHS. (The abbreviations of DMF, PVDF, and NMP correspond to *N*,*N*′-dimethylformamide, poly(vinylidene fluoride), and *N*-methylpyrrolidone, respectively.)

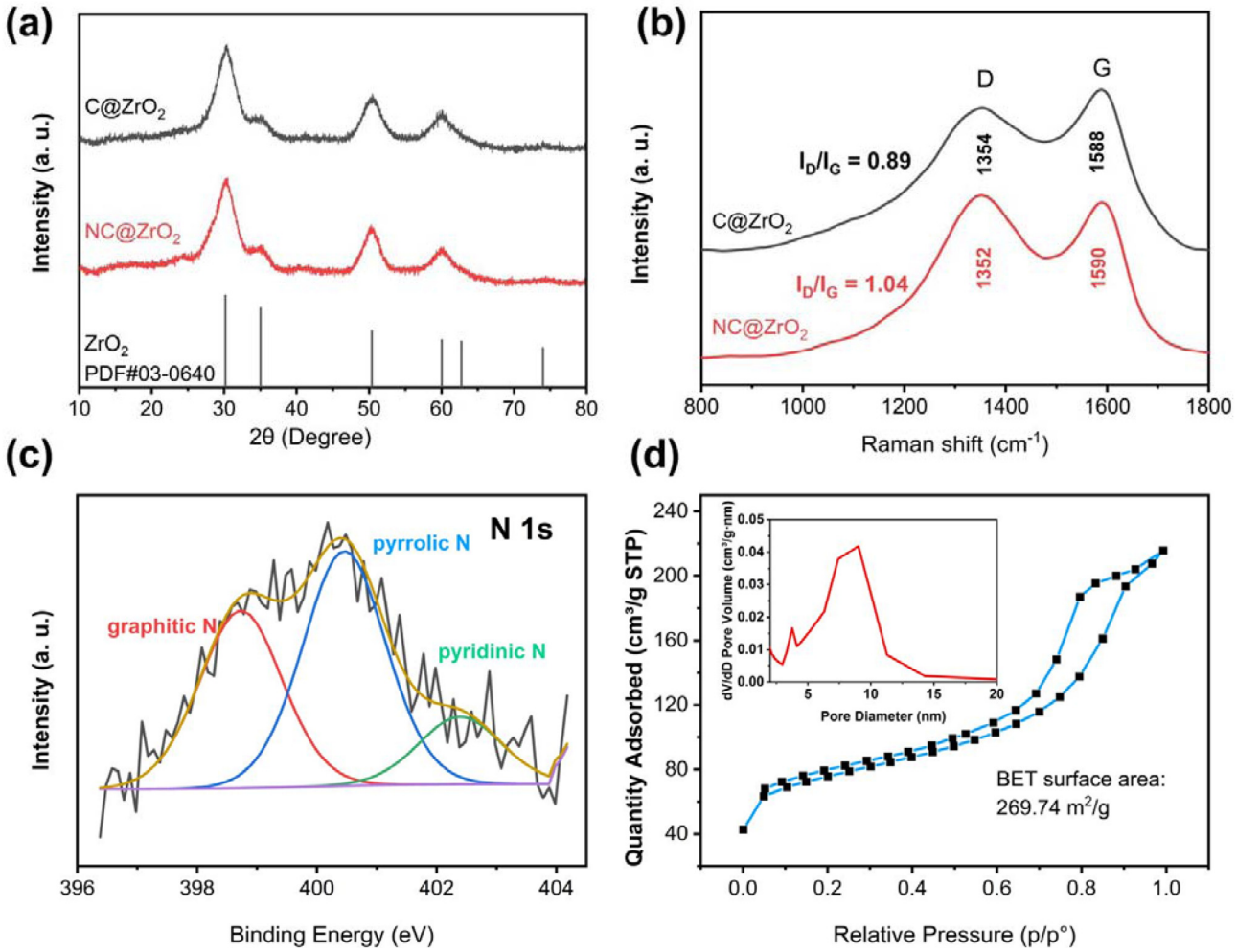

Fig. 2 Materials characterization of the NC@ZrO_2 composite. (a) XRD and (b) Raman spectra of NC@ZrO_2 and C@ZrO_2 composites. (c) N 1s high-resolution XPS spectra of the NC@ZrO_2 composite. (d) N_2 adsorption and desorption curves of the NC@ZrO_2 composite; the inset shows the pore size distribution.

indicates a high degree of disorder and a large population of defects in the graphitic lattices of the NC@ZrO_2 composite. These results manifest that introducing of N heteroatoms brings efficient lattice defects, leading to additional active sites and better adsorption properties, which is beneficial for Zn^{2+} storage. Moreover, N doping can not only increase the electrical conductivity, but also improve the electrolyte infiltration;[5] all these merits will facilitate the electrochemical performance of the NC@ZrO_2 composite.

Furthermore, X-ray photoelectron spectroscopy (XPS) was conducted to characterize the surface chemical composition of NC@ZrO_2. The C 1s spectrum (Fig. S2†) can be deconvoluted into three peaks. The dominant peak at 284.75 eV is related to the C–C configuration, while the peaks at 286.45 eV (C–N) and 288.51 eV (C–O) are ascribed to the surface oxygen and nitrogen groups, respectively. The N 1s spectrum of NC@ZrO_2 consists of three distinct peaks at 402.5, 400.46, and 398.73 eV (Fig. 2c), which are attributed to the graphitic-N, pyrrolic-N, and pyridinic-N, respectively.[27] The different nitrogen species observed in the N 1s spectrum further demonstrate the successful doping of carbon with heteroatoms, which can optimize the electronic properties of carbon-based cathodes.

Furthermore, the pore structure of NC@ZrO_2 and C@ZrO_2 composites was characterized by the Brunauer–Emmett–Teller (BET) nitrogen adsorption/desorption technique. The NC@ZrO_2 composite delivers a BET surface area of 269.74 m^2 g^{-1} (Fig. 2d), even higher than that of the C@ZrO_2 composite (169.82 m^2 g^{-1}, Fig. S3a†). Furthermore, the Barrett–Joyner–Halenda (BJH) pore size distribution of NC@ZrO_2 reveals a hierarchical porous structure with the pore size ranging from 3 nm to 10 nm (inset of Fig. 2d). In contrast, C@ZrO_2 shows a narrow pore-size distribution (Fig. S3b†), with the pore size centered at 3.73 nm. The relatively larger surface area promotes chemical adsorption, while the hierarchical porous structure is favorable for Zn^{2+} transport, which benefits the electrochemical properties in terms of higher specific capacity and better rate capability.

The microstructures of different samples are further evaluated by scanning electron microscopy (SEM) and transmission electron microscopy (TEM) observations. The as-prepared

UiO-66 (Fig. S4a†) exhibits a polyhedron shape with the particle size ranging from 100 nm to 3 μm. The shape of UiO-66-NH_2 is similar to that of UiO-66; however, the size of the particles is much smaller, with the average size of ~80 nm (Fig. S4b†), which corresponds to broad XRD peaks (Fig. S1†), and the nano-sized primary particles loosely aggregate together to form micron-sized secondary blocky-shaped particles. After pyrolysis and acid etching, the formed secondary particles of the NC@ZrO_2 composite mainly comprise small spheres with an average size of ~3 nm (Fig. 3a–c and S4c†), which is evenly distributed and also loosely packed. While the C@ZrO_2 composite retains its bulky polyhedron shape (Fig. S4d†), small compact spheres are also observed inside the polyhedra (Fig. S5b†). High-resolution transmission electron microscopy (HRTEM) images (Fig. 3d) further show that the interplanar spacing of the small spheres is 0.29 nm, corresponding well to the (111) plane of ZrO_2. The ZrO_2 spheres distribute homogeneously among the amorphous carbon framework, which benefits the interfacial interaction between the electrolyte and cathode materials. Furthermore, the energy dispersive spectroscopy (EDS) spectrum confirms the homogeneous distribution of C, N, O and Zr elements (Fig. 3e), and the mass ratio is 53.58%, 2.95%, 34.42%, and 9.05%, respectively. While for the C@ZrO_2 composite, ZrO_2 spheres are also verified by HRTEM (Fig. S5b†), no N element was detected by EDS (Fig. S5c†), and the content of other elements is similar to NC@ZrO_2. The above results indicate that a hierarchical architecture with N-doped porous C and evenly distributed nano-sized ZrO_2 has been successfully built in the NC@ZrO_2 composite. Compared with the C@ZrO_2 composite, the primary nano-sized ZrO_2 spheres are loosely packed and surrounded by N-doped C, which provides abundant channels for electrolyte and ion transport and favors better electrochemical properties. In contrast, for the large C@ZrO_2 polyhedra, the compact

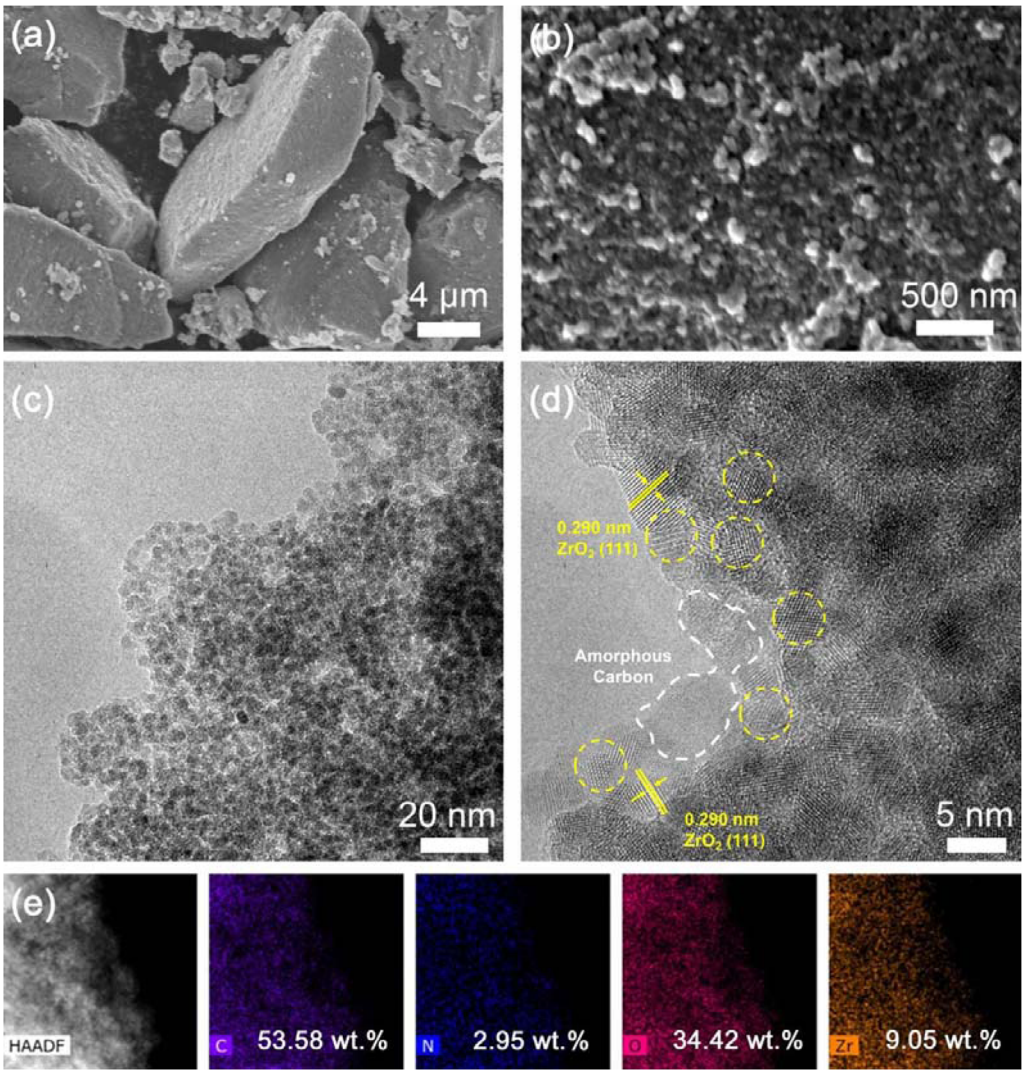

Fig. 3 Morphology characterization of the NC@ZrO_2 composite. (a) and (b) SEM images, (c) TEM image, (d) HRTEM image, and (e) TEM EDS elemental mapping of the NC@ZrO_2 composite, and the mass ratio of C, N, O, and Zr.

structure results in lower efficiency of mass and charge transfer inside the particles, leading to attenuated electrochemical properties.

To determine the ZrO_2 content in the composites, TG-DTA experiment under an oxidizing atmosphere was carried out, to convert the C and N elements into CO_x and NO_x and then remove the products. The weight losses of NC@ZrO_2 and C@ZrO_2 composites are 38.43% and 41.45%, respectively (Fig. S6a and b†), indicating that the original ZrO_2 content in these two samples is about 61.57% and 58.55% respectively when assuming that the water absorption is negligible.

3.2 Electrochemical performance

The electrochemical performance of the NC@ZrO_2 cathode for ZHSs was assessed in the electrolyte 2 M $ZnSO_4$. First, cyclic voltammetry (CV) curves with cut-off voltages ranging from 1.6 to 2.1 V were used to determine the optimal operating voltage (Fig. 4a). The CV curves are approximately symmetrical with a cut-off voltage lower than 1.8 V, while the forward current increases significantly with higher cut-off voltages. The above results suggest that the ideal operating voltage for ZHSs with the NC@ZrO_2 cathode was 0.1–1.8 V. Similarly, the voltage

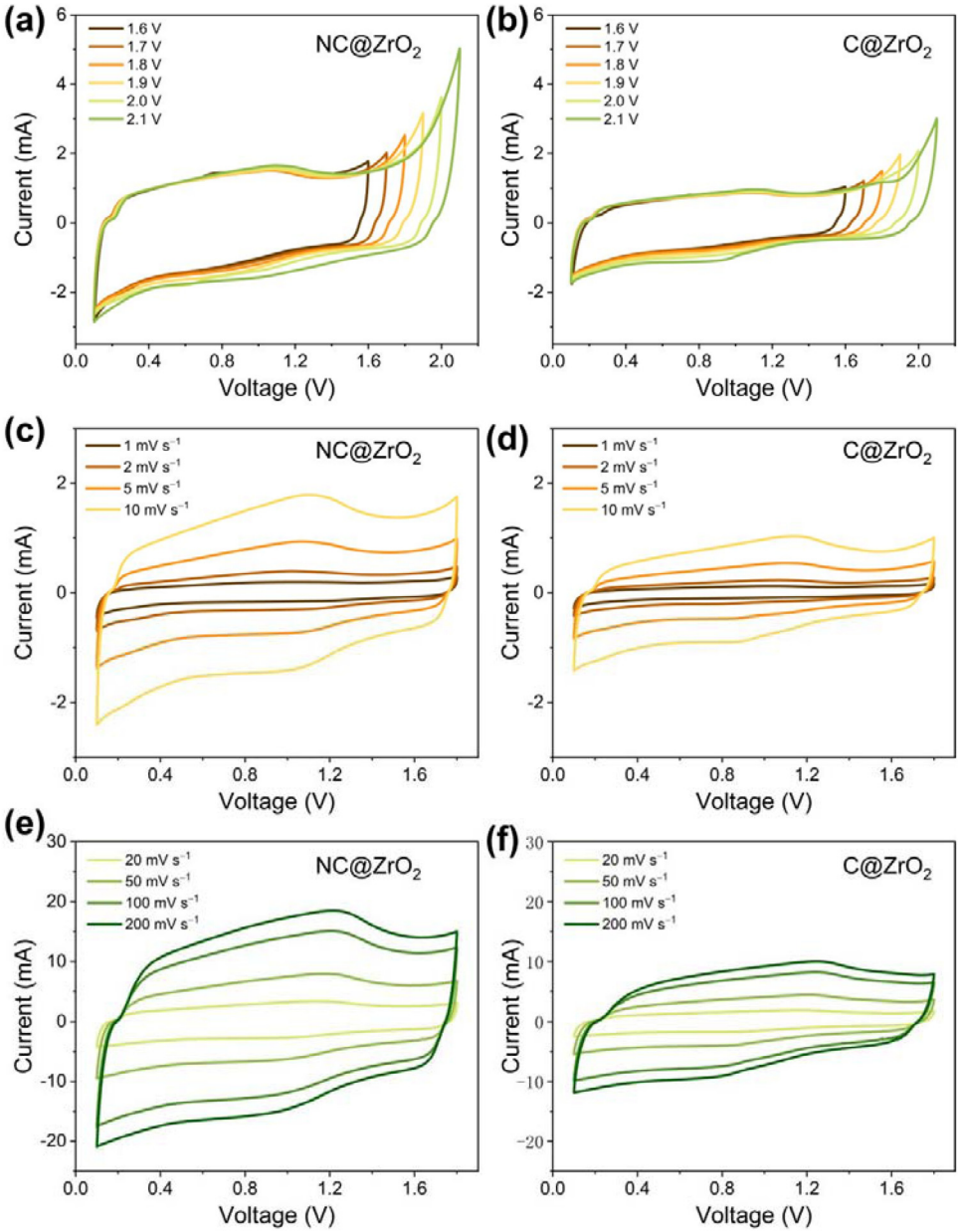

Fig. 4 Electrochemical performance of the NC@ZrO_2 and the C@ZrO_2 composites. CV curves with cut-off voltages ranging from 1.6 to 2.1 V of (a) NC@ZrO_2 and (b) C@ZrO_2 cathode. (c) and (e) CV curves at various scan rates of the NC@ZrO_2 cathode. (d) and (f) CV curves at various scan rates of the C@ZrO_2 cathode.

window of C@ZrO_2 also was determined to be 0.1–1.8 V (Fig. 4b). Subsequently, the CV curves of NC@ZrO_2 at various scan rates are presented in Fig. 4c and e. The curves retain a quasi-rectangular shape with larger distortion, indicating a combination of the electric double-layer capacitor of the carbon framework and the pseudocapacitive behaviors of ZrO_2. Furthermore, compared with the C@ZrO_2 cathode (Fig. 4d and f), the NC@ZrO_2 cathode still exhibits a similar shape of the CV curve even at a super-fast scan rate of 200 mV s^{-1}, which demonstrated that the remarkable rate capability of the Zn-NC@ZrO_2 capacitor stems from the introduction of the nitrogen element.

Due to the pseudocapacitive properties of ZrO_2, there is a relatively obvious redox peak around 1.0 V in the CV curve (Fig. S7a†). To further clarify the electrochemical kinetics of the NC@ZrO_2 and C@ZrO_2 electrodes, the capacitive and redox pseudocapacitance-like contribution was analyzed. As disclosed in Fig. S7b,† the *b* values of the anodic and cathodic

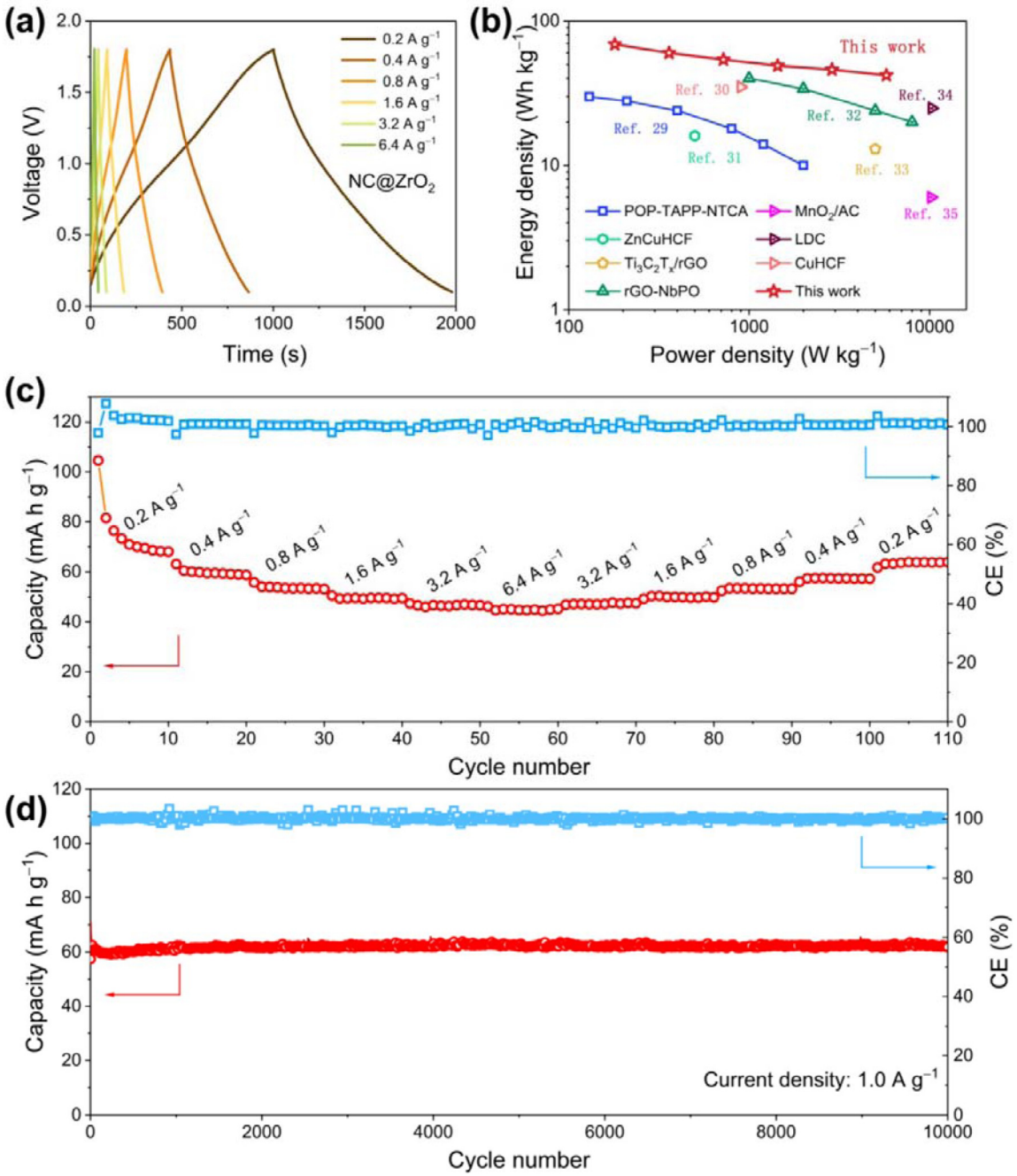

Fig. 5 Electrochemical performance of NC@ZrO_2 and C@ZrO_2 composite based ZHSs. (a) GCD curves of NC@ZrO_2 based ZHS at current ranging from 0.2 to 6.4 A g^{-1}. (b) The Ragone plot comparison between different supercapacitors and NC@ZrO_2 based ZHSs. (c) Rate properties of NC@ZrO_2-based ZHS. (d) Cycling performance of NC@ZrO_2-based ZHS.

peaks are 0.96 and 0.95, respectively, indicating that the storage kinetics of NC@ZrO_2 is a combination of pseudocapacitive and capacitive mechanisms. The contributions to the capacity were further quantified; with increasing scan rate, the capacitive contribution ratio becomes higher and the ratio value reaches 90.4% at a scan rate of 10 mV s^{-1} (Fig. S7c and d†). Similarly, the capacitive contribution ratio of the C@ZrO_2 electrode was calculated to be 88.7% at a scan rate of 10 mV s^{-1} (Fig. S8c and d†). Such a high capacitance ratio of the NC@ZrO_2 can lead to faster ion adsorption for better rate performance.

The galvanostatic charge and discharge (GCD) curves of NC@ZrO_2-based ZHSs at different current densities ranging from 0.2 to 6.4 A g^{-1} are shown in Fig. 5a. All the curves were symmetric and linear in shape, agreeing well with the results from CV curves. It is noted that the GCD curves of C@ZrO_2-based ZHS at different current rates are slightly different from that of the NC@ZrO_2-based ZHS (Fig. S9†). The charging curve of C@ZrO_2-based ZHS has a lower slope in the high-voltage region due to the severe self-discharge behavior. In contrast, the GCD curve of the NC@ZrO_2-based ZHS shows a more symmetrical shape and exhibits better resistance to self-discharge. Notably, the NC@ZrO_2-based ZHS shows a remarkable energy density of 69 W h kg^{-1} at a power density of 180 W kg^{-1} and also retains an energy density of 42 W h kg^{-1} when the power density increased to 5760 W kg^{-1}, which is superior to that of most reported materials[29–35] (Fig. 5b). Markedly, the NC@ZrO_2 cathode can deliver reversible capacities of 81.5, 60.5, 54.0, 49.4, 46.6, and 45.0 mA h g^{-1} at 0.2, 0.4, 0.8, 1.6, 3.2, and 6.4 A g^{-1}, respectively. When the current density recovers to 0.2 A g^{-1}, it could restore to a capacity of 63.9 mA h g^{-1} (Fig. 5c). The rate performance of the NC@ZrO_2 cathode is much better than that of the C@ZrO_2 cathode (Fig. S10†), which can be attributed to nitrogen doping which improves the overall conductivity. The long-term cycling performance of the NC@ZrO_2-based ZHS was studied at the current density of 1.0 A g^{-1}, as displayed in Fig. 5d. The NC@ZrO_2-based ZHS shows an initial capacity of 64.2 mA h g^{-1} with retention of 97.7% and almost 100% coulombic efficiency (CE) after 10 000 cycles. In contrast, the C@ZrO_2-based ZHS could only exhibit an initial capacity of 38.4 mA h g^{-1} and a short lifespan of 4100 cycles (Fig. S11†). Overall, the electrochemical performance of NC@ZrO_2 is much better than that of C@ZrO_2. This can be attributed to the stronger electronegativity of N element than that of C, which can accommodate the adsorption of more zinc ions, resulting in an enhanced capacity.

Anti-self-discharge ability has become an important indicator for evaluating ZHSs. Our constructed NC@ZrO_2-based ZHS exhibits excellent performance towards anti-self-discharge. As disclosed in Fig. 6a, NC@ZrO_2-based ZHS was rested for 24 hours after being charged to 100% state of charge (SOC). Then, the battery was discharged to 0% SOC, delivering a capacity of 81.5%. Such superior anti-self-discharge may be attributed to the synergistic effect between N-doping porous carbon and pseudocapacitive ZrO_2. Compared with conventional supercapacitors,[36–42] zinc-based hybrid capacitors exhibit a higher capability of anti-self-discharge (Fig. 6b).

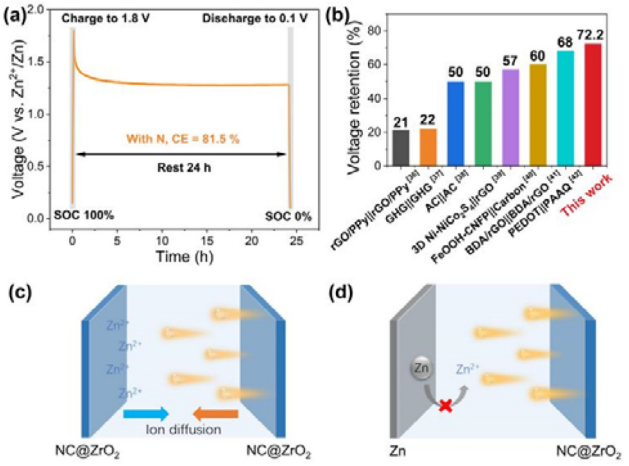

Fig. 6 Anti-self-discharge analysis of NC@ZrO_2-based ZHS. (a) Self-discharge curve of NC@ZrO_2-based ZHS. (b) The capacitance retention of different supercapacitors and ion hybrid capacitor systems. (CE is the abbreviation of capacitance retention.) (c) and (d) The schematic diagrams of NC@ZrO_2-based symmetric supercapacitors and ZHS in the charged state.

The schematic diagrams of NC@ZrO_2-based symmetric supercapacitors and ZHSs in the charged state are shown in Fig. 6c and d, respectively. In the symmetric supercapacitors (Fig. 6c), NC@ZrO_2 is used as both the anode and cathode materials, which store energy through adsorption and pseudocapacitive behavior. In the fully charged state, anions are adsorbed on the surface of the cathode and Zn^{2+} ions are adsorbed on the surface of the anode. Due to the different concentrations and voltages between electrodes and the electrolyte, adsorbed ions on the electrode surface tend to diffuse autonomously into the electrolyte under open-circuit conditions. Therefore, NC@ZrO_2-based symmetric supercapacitors exhibit higher self-discharge rates. In contrast, the reaction mechanism for ZHSs is different (Fig. 6d). During the charging and discharging process, the conversion reaction between Zn and Zn^{2+} occurs at the anode; at the same time, adsorption and pseudocapacitive reactions occur on the surface of the cathode. Therefore, there is no cation concentration difference in the negative electrode of the ZHSs, and the possibility of zinc spontaneously converting to zinc ions in the open-circuit state is low. The movement rate of zinc ions is also slower than the self-diffusion speed of adsorbed ions. As a result, NC@ZrO_2-based ZHS can exhibit excellent anti-self-discharge performance.

4. Conclusions

In this work, an N-doped porous carbon framework with homogeneously distributed nano-sized ZrO_2 particles was designed as the cathode material for ZHSs. The introduction of heteroatoms in the carbon framework and ZrO_2 nanoparticles with pseudocapacitive reactions demonstrate the pro-

moted chemical adsorption and the accelerated Zn^{2+}-storage kinetics. As a result, the NC@ZrO_2 cathode delivers impressive electrochemical properties in terms of excellent capacitance and good rate capability. A remarkable maximum energy density of 69 W h kg^{-1} and a maximum power density of 5760 W kg^{-1} can be achieved in the NC@ZrO_2-based ZHSs. Moreover, the NC@ZrO_2-based ZHSs demonstrate an ultralong lifespan (10 000 cycles) and superior anti-self-discharge behavior (81.5% of capacitance retention after 24 h). This work provides a high-performance cathode material for ZHSs and inspires new thoughts on advanced electrode design for ZHSs toward practical applications.

Conflicts of interest

There are no conflicts of interest to declare.

Acknowledgements

The authors acknowledge the financial support by the National Natural Science Foundation of China (Grant No. 21971017), the China National Petroleum Corporation Research Fund Program, and the Research Institute of Petroleum Exploration and Development Research Fund Program.

References

1 Y. Liang, H. Dong, D. Aurbach and Y. Yao, Current status and future directions of multivalent metal-ion batteries, *Nat. Energy*, 2020, **5**(9), 646–656.
2 F. Wang, O. Borodin, T. Gao, X. Fan, W. Sun, F. Han, A. Faraone, J. A. Dura, K. Xu and C. Wang, Highly reversible zinc metal anode for aqueous batteries, *Nat. Mater.*, 2018, **17**(6), 543–549.
3 W. Sun, F. Wang, B. Zhang, M. Zhang, V. Küpers, X. Ji, C. Theile, P. Bieker, K. Xu, C. Wang and M. Winter, A rechargeable zinc-air battery based on zinc peroxide chemistry, *Science*, 2021, **371**(6524), 46–51.
4 X. Jia, C. Liu, Z. G. Neale, J. Yang and G. Cao, Active materials for aqueous zinc ion batteries: synthesis, crystal structure, morphology, and electrochemistry, *Chem. Rev.*, 2020, **120**(15), 7795–7866.
5 L. Wang, M. Peng, J. Chen, T. Hu, K. Yuan and Y. Chen, Eliminating the micropore confinement effect of carbonaceous electrodes for promoting Zn-ion storage capability, *Adv. Mater.*, 2022, **34**, 2203744.
6 Z. Huang, T. Wang, H. Song, X. Li, G. Liang, D. Wang, Q. Yang, Z. Chen, L. Ma, Z. Liu, B. Gao, J. Fan and C. Zhi, Effects of anion carriers on capacitance and self-discharge behaviors of zinc ion capacitors, *Angew. Chem. Int. Ed.*, 2021, **60**(2), 1011–1021.
7 Z. Xu, M. Li, W. Sun, T. Tang, J. Lu and X. Wang, An ultrafast, durable, and high-loading polymer anode for aqueous zinc-ion batteries and supercapacitors, *Adv. Mater.*, 2022, **34**(23), 2200077.
8 Z. Huang, A. Chen, F. Mo, G. Liang, X. Li, Q. Yang, Y. Guo, Z. Chen, Q. Li, B. Dong and C. Zhi, Phosphorene as cathode material for high-voltage, anti-self-discharge zinc ion hybrid capacitors, *Adv. Energy Mater.*, 2020, **10**(24), 2001024.
9 J. Jin, X. Geng, Q. Chen and T. Ren, A better Zn-ion storage device: recent progress for Zn-ion hybrid supercapacitors, *Nano-Micro Lett.*, 2022, **14**(1), 64–64.
10 L. Dong, X. Ma, Y. Li, L. Zhao, W. Liu, J. Cheng, C. Xu, B. Li, Q. Yang and F. Kang, Extremely safe, high-rate and ultralong-life zinc-ion hybrid supercapacitors, *Energy Storage Mater.*, 2018, **13**, 96–102.
11 J. Yin, W. Zhang, N. A. Alhebshi, N. Salah and H. N. Alshareef, Electrochemical zinc ion capacitors: fundamentals, materials, and systems, *Adv. Energy Mater.*, 2021, **11**(21), 2100201.
12 H. Yu, Q. Li, W. Liu, H. Wang, X. Ni, Q. Zhao, W. Wei, X. Ji, Y. Chen and L. Chen, Fast ion diffusion alloy layer facilitating 3D mesh substrate for dendrite-free zinc-ion hybrid capacitors, *J. Energy Chem.*, 2022, **73**, 565–574.
13 Q. Liu, H. Zhang, J. Xie, X. Liu and X. Lu, Recent progress and challenges of carbon materials for Zn-ion hybrid supercapacitors, *Carbon Energy*, 2020, **2**(4), 521–539.
14 H. Wang, Y. Chen, H. Yu, W. Liu, G. Kuang, L. Mei, Z. Wu, W. Wei, X. Ji, B. Qu and L. Chen, A multifunctional artificial interphase with fluorine-doped amorphous carbon layer for ultra-stable Zn anode, *Adv. Funct. Mater.*, 2022, **32**(43), 2205600.
15 H. Yu, Y. Chen, H. Wang, X. Ni, W. Wei, X. Ji and L. Chen, Engineering multi-functionalized molecular skeleton layer for dendrite-free and durable zinc batteries, *Nano Energy*, 2022, **99**, 107426.
16 W. Fan, J. Ding, J. Ding, Y. Zheng, W. Song, J. Lin, C. Xiao, C. Zhong, H. Wang and W. Hu, Identifying heteroatomic and defective sites in carbon with dual-ion adsorption capability for high energy and power zinc ion capacitor, *Nano-Micro Lett.*, 2021, **13**(1), 59–59.
17 M. R. Lukatskaya, S. Kota, Z. Lin, M. Zhao, N. Shpigel, M. D. Levi, J. Halim, P. Taberna, M. W. Barsoum, P. Simon and Y. Gogotsi, Ultra-high-rate pseudocapacitive energy storage in two-dimensional transition metal carbides, *Nat. Energy*, 2017, **2**(8), 17105–17112.
18 Q. Meng, K. Cai, Y. Chen and L. Chen, Research progress on conducting polymer based supercapacitor electrode materials, *Nano Energy*, 2017, **36**, 268–285.
19 J. Han, K. Wang, W. Liu, C. Li, X. Sun, X. Zhang, Y. An, S. Yi and Y. Ma, Rational design of nano-architecture composite hydrogel electrode towards high performance Zn-ion hybrid cell, *Nanoscale*, 2018, **10**(27), 13083–13091.
20 X. Yang, Q. Wang, K. Zhu, K. Ye, G. Wang, D. Cao and J. Yan, 3D porous oxidation-resistant MXene/graphene architectures induced by In situ zinc template toward high-performance supercapacitors, *Adv. Funct. Mater.*, 2021, **31**(20), 2101087.

21 H. Wang, W. Ye, Y. Yang, Y. Zhong and Y. Hu, Zn-ion hybrid supercapacitors: achievements, challenges and future perspectives, *Nano Energy*, 2021, **85**, 105942.
22 C. Gautam, J. Joyner, A. Gautam, J. Rao and R. Vajtai, Zirconia based dental ceramics: structure, mechanical properties, biocompatibility and applications, *Dalton Trans.*, 2016, **45**(48), 19194–19215.
23 W. Zhang, Y. Tan, Y. Gao, J. Wu and B. Tang, Ultrafine nano zirconia as electrochemical pseudocapacitor material, *Ceram. Int.*, 2015, **41**(2), 2626–2630.
24 L. Wang, M. Peng, J. Chen, X. Tang, L. Li, T. Hu, K. Yuan and Y. Chen, High energy and power zinc ion capacitors: a dual-ion adsorption and reversible chemical adsorption coupling mechanism, *ACS Nano*, 2022, **16**(2), 2877–2888.
25 J. H. Cavka, S. Jakobsen, U. Olsbye, N. Guillou, C. Lamberti, S. Bordiga and K. P. Lillerud, A new zirconium inorganic building brick forming metal organic frameworks with exceptional stability, *J. Am. Chem. Soc.*, 2008, **130**(42), 13850–13851.
26 S. Liu, Z. Yue and Y. Liu, Mesoporous carbon-ZrO_2 composites prepared using thermolysis of zirconium based metal-organic frameworks and their adsorption properties, *J. Porous Mater.*, 2015, **22**(2), 465–471.
27 J. Zhang, X. Dong, W. Xing, Y. Luo, Y. Chen, Y. Xue, C. Zhang, J. Chen, G. Wang and R. Wang, Engineering iron single atomic sites with adjacent ZrO_2 nanoclusters via ligand-assisted strategy for effective oxygen reduction reaction and high–performance Zn-air batteries, *Chem. Eng. J.*, 2021, **420**, 129938.
28 P. Pachfule, D. Shinde, M. Majumder and Q. Xu, Fabrication of carbon nanorods and graphene nanoribbons from a metal-organic framework, *Nat. Chem.*, 2016, **8**(7), 718–724.
29 F. Cui, Z. Liu, D. Ma, L. Liu, T. Huang, P. Zhang, D. Tan, F. Wang, G. Jiang and Y. Wu, Polyarylimide and porphyrin based polymer microspheres for zinc ion hybrid capacitors, *Chem. Eng. J.*, 2021, **405**, 127038.
30 R. Trócoli and F. La Mantia, An aqueous zinc-ion battery based on copper hexacyanoferrate, *ChemSusChem*, 2015, **8**(3), 481–485.
31 G. Kasiri, J. Glenneberg, A. Bani Hashemi, R. Kun and F. La Mantia, Mixed copper-zinc hexacyanoferrates as cathode materials for aqueous zinc-ion batteries, *Energy Storage Mater.*, 2019, **19**, 360–369.
32 S. J. Patil, N. R. Chodankar, S. Hwang, G. S. R. Raju, K. S. Ranjith, Y. S. Huh and Y. Han, Ultra-stable flexible Zn-ion capacitor with pseudocapacitive 2D layered niobium oxyphosphides, *Energy Storage Mater.*, 2022, **45**, 1040–1051.
33 Q. Wang, S. Wang, X. Guo, L. Ruan, N. Wei, Y. Ma, J. Li, M. Wang, W. Li and W. Zeng, MXene-reduced graphene oxide aerogel for aqueous zinc-ion hybrid supercapacitor with ultralong cycle life, *Adv. Electron. Mater.*, 2019, **5**(12), 1900537.
34 Y. Lu, Z. Li, Z. Bai, H. Mi, C. Ji, H. Pang, C. Yu and J. Qiu, High energy-power Zn-ion hybrid supercapacitors enabled by layered B/N co-doped carbon cathode, *Nano Energy*, 2019, **66**, 104132.
35 X. Ma, J. Cheng, L. Dong, W. Liu, J. Mou, L. Zhao, J. Wang, D. Ren, J. Wu, C. Xu and F. Kang, Multivalent ion storage towards high-performance aqueous zinc-ion hybrid supercapacitors, *Energy Storage Mater.*, 2019, **20**, 335–342.
36 A. Jana, E. Scheer and S. Polarz, Synthesis of graphene-transition metal oxide hybrid nanoparticles and their application in various fields, *Beilstein J. Nanotechnol.*, 2017, **8**, 688–714.
37 L. Chen, Y. Chen, J. Wu, J. Wang, H. Bai and L. Li, Electrochemical supercapacitor with polymeric active electrolyte, *J. Mater. Chem. A*, 2014, **2**(27), 10526–10531.
38 D. Momodu, A. Bello, K. Oyedotun, F. Ochai-Ejeh, J. Dangbegnon, M. Madito and N. Manyala, Enhanced electrochemical response of activated carbon nanostructures from tree-bark biomass waste in polymer-gel active electrolytes, *RSC Adv.*, 2017, **7**(59), 37286–37295.
39 B. Saravanakumar, S. S. Jayaseelan, M. K. Seo, H. Y. Kim and B. S. Kim, $NiCo_2S_4$ nanosheet-decorated 3D, porous Ni film@Ni wire electrode materials for all solid-state asymmetric supercapacitor applications, *Nanoscale*, 2017, **9**(47), 18819–18834.
40 T. Nguyen and M. Fátima Montemor, γ-FeOOH and amorphous Ni-Mn hydroxide on carbon nanofoam paper electrodes for hybrid supercapacitors, *J. Mater. Chem. A*, 2018, **6**(6), 2612–2624.
41 B. Song, J. Zhao, M. Wang, J. Mullavey, Y. Zhu, Z. Geng, D. Chen, Y. Ding, K. Moon, M. Liu and C. Wong, Systematic study on structural and electronic properties of diamine/triamine functionalized graphene networks for supercapacitor application, *Nano Energy*, 2017, **31**, 183–193.
42 F. N. Ajjan, M. Vagin, T. Rębiś, L. E. Aguirre, L. Ouyang and O. Inganäs, Scalable asymmetric supercapacitors based on hybrid organic/biopolymer electrodes, *Adv. Sustainable Syst.*, 2017, **1**(8), 1700054.

